A CMOS compatible micro-Pirani vacuum sensor based on mutual heat transfer with 5-decade operating range and 0.3 Pa detection limit

Massimo Piotto[a], Simone Del Cesta[b], Paolo Bruschi[b]

[a]IEIIT-PISA, CNR, Via G. Caruso 16, 56122 Pisa, Italy
[b]Dipartimento di Ingegneria dell'Informazione, University of Pisa, Via G. Caruso 16, 56122 Pisa, Italy

Abstract

A Pirani vacuum sensor based on mutual heating between a heater and a distinct temperature probe, separated by a 5 μm air gap, is proposed. The sensor is fabricated by applying a simple post-processing procedure to chips designed and fabricated using the BCD6s process (Bipolar-CMOS-DMOS) of STMicroelectronics. The sensor layout has been optimized to exploit the layers of the original process in order to enhance the sensor performance. The sensors exhibit a resolution better than 0.4 Pa from nearly 0.3 Pa to 1 kPa and better than 50 Pa from 1 kPa to 100 kPa. The sensor response at the lower extreme of the pressure interval is marked by an offset voltage, which is three orders of magnitude smaller than the full-scale value. Finite Element Method simulations suggest that the offset is due to pressure-independent heat transfer due to radiation and conduction through the substrate. The simulated equivalent offset drift is 50 mPa / K.

Keywords: Micro-Pirani; MEMS; CMOS compatible; wide pressure range; FEM simulation.

Corresponding Author:

Prof. Paolo Bruschi
Università di Pisa
Dipartimento di Ingegneria dell'Informazione
via Caruso, 16 56122 Pisa, Italy
tel. +39 050 2217538
fax. +39 050 2217522
e-mail: p.bruschi@iet.unipi.it

1. Introduction

Vacuum sensors [1] are essential for the correct operation of many manufacturing apparatuses, especially in the field of integrated circuit fabrication. Vacuum monitoring is also of great importance when a condition of medium or high vacuum is required to guarantee effective thermal insulation, such as in cryogenic systems and thermodynamic solar power plants [2]. Vibrational Micro Electro Mechanical Systems (MEMS) should be packaged in vacuum to reduce mechanical damping [3-5]. For these devices, in-package vacuum monitoring is desirable to detect sealing failure. In most of the mentioned applications, the vacuum range of interest (~10^{-2}Pa-10kPa) can be covered with a Pirani vacuum gauge, which is based on the effects exerted by pressure on the thermal conductance of an air gap. This kind of sensors is particularly suitable to be fabricated by means of micromachining technologies, obtaining advantages in terms of miniaturization, power consumption, response speed and range. These characteristics allow in-package vacuum sensing and pave the way to emerging applications such as distributed vacuum monitoring in large industrial plants by means of wireless sensor networks or RF-ID tags.

The first MEMS Pirani-like vacuum sensors were proposed starting from the mid-eighties [6]. Since then, an impressive number of different designs have been proposed in the literature [7-21], while commercial applications have begun to appear in last decade [22]. Exploitation of standard IC (integrated circuit) fabrication technologies, followed by micromachining steps (post-processing), to produce MEMS Pirani sensors has been proposed and demonstrated since the first pioneering works [6-9], resulting in a viable approach to reduce development and production costs and integrate the sensors on the same substrate as the readout electronic interfaces [9-11]. Miniaturization allowed improving also the typically very low sensitivity exhibited by traditional Pirani gauges at atmospheric pressure, since the shorter the air gap, the higher the pressure at which the sensitivity starts to drop. Gaps of a few microns are sufficient to obtain acceptable performances up to atmospheric pressure [8], while extension of the operating range up to even higher pressures can be obtained pushing some dimensions down to the nanometer region [20,21].

On the other hand, the lower end of the pressure operating range is determined by two main issues: noise and offset drift. Noise originates in the sensor elements (e.g. Johnson noise) and in the readout amplifiers. The offset (i.e. the output signal for zero pressure) is typically dominated by the sensor contribution. In next section, we will recall the self-heating and mutual-heating configurations [8]. The self-heating configuration replicates the structure of traditional Pirani gauges and is by far the most used. Its main drawback is the large offset value, which, being affected by significant temperature drift, requires compensation schemes [7, 18]. These techniques require precise calibration and are prone to significant residual errors. Temperature stabilization of the whole sensing chip may be an effective solution [12], but it leads to significant increase of the device size and power consumption. The offset issue can be effectively mitigated using the mentioned mutual heating configuration, in which the output signal is proportional to the heat conveyed across the air gap, so that it tends to zero with pressure, at least in principle. In practice, even for this configuration there is a residual offset, although it is much smaller than in the self-heating configuration. Since the first time it was proposed by Paul et al. [8], the mutual heating configuration has received very little interest. Recently, we have used the principle of mutual heat transfer between distinct heaters and temperature probes to develop integrated flow sensors capable of self-compensating the cross-sensitivity to pressure [23-24] or providing independent readings of pressure and flow from a single sensor [24].

In this work, we describe the fabrication, experimental characterization and modeling of a Pirani sensor, based on the mutual heating configuration. The device relies on a commercial microelectronic process for most part of its fabrication flow, requiring only a simple post-processing finishing procedure, which involves a single low-resolution photolithographic step. This choice was made to make the whole sensor development flow affordable for University labs and Small-Medium Enterprises.

The sensing structure consists of a heater and a temperature probe, placed on two different cantilever beams separated by a small air gap. The available layers of the original microelectronic process have been combined to optimize the key parameters of the device: in particular, the cross section of the air gap has been maximized for improved sensitivity, while the thickness of the heater cantilever was reduced to limit power consumption. The pressure-sensing structures have been integrated on a test chip that includes also different kind of sensors, which are not relevant for this work, and a low noise, low offset integrated readout interface, which has been effectively used to read the sensor output voltage. Preliminary results were presented in [25]. In this work, we propose new measurements aimed at investigating a few issues that can play a key role in determining the actual performances of operating range, accuracy and resolution. In particular, the response of two symmetrical sensing structures present on the same test chip are compared to determine the degree of matching that can be obtained between distinct sensors. Furthermore, the origin of the residual offset is investigated with the aid of FEM (Finite Element Method) simulations performed using COMSOL Multiphysics.

2. Device description and fabrication

2.1) Principle of operation

Let us consider two parallel surfaces at temperature T_1 and T_2, respectively, separated by a gap of length d, filled by a gas. The heat flow from one surface to the other can be approximated by the following linear relationship:

$$Q_{12} = G_{gap}(T_1 - T_2) \tag{1}$$

where G_{gap} is the thermal conductance of the gap, which exhibits a dependence on the gas pressure given by:

$$G_{gap} = \frac{G_0}{1 + p_{tr}/p} \tag{2}$$

where G_0 is the asymptotic limit for an infinite pressure, while p_{tr} is a parameter called transition pressure. The transition pressure depends on the gas type, on the surface composition and generally exhibits an inverse proportionality to the gap length [8]. This phenomenon is the basis of the Pirani type pressure sensors. Two possible configurations that can be used to build Pirani-type MEMS pressure sensors (micro-Pirani) are shown in Fig. 1 (a) and Fig.1 (b), respectively. The former consists of a cantilever separated from the substrate by a short air gap (length d), and equipped with a heater and a temperature sensor, which may coincide with a single temperature-dependent resistor. The heater dissipates a constant power creating a temperature difference (overheating) between the cantilever and the substrate. The overheating is proportional to the inverse of total thermopile-substrate conductance, which includes pressure dependent components such as G_{gap}. In the second configuration, shown in Fig. 1(b), heater and temperature probe are placed on distinct cantilevers, laterally separated by the air gap. In this case, the overheating measured by the temperature sensor is proportional to mutual heat transfer between the membranes, which is proportional to G_{gap}.

Most of micro-Pirani pressure gauges presented in the literature are based on the self-heating configuration represented in Fig. 1(a). The main drawback of this approach is that the overheating tends to a very large constant value when the pressure tends to zero. This value is prone to drifts due to room temperature variations, and ageing of the sensor structure. Even small relative variations may result in large errors in the measured pressure. The consequence is reduced capability of

detecting small pressures. On the other hand, the mutual heating structure of Fig. 1(b) is marked by an overheating of the temperature probe, ΔT, given by:

$$\Delta T = \frac{G_{gap}}{G_{gap} + G_S} W_H \cong \frac{G_{gap}}{G_S} W_H \tag{3}$$

where W_H is the heater power, while G_S is the total conductance from the cantilever tip and the ambient (considered at uniform temperature, equal to the chip substrate temperature). The approximation made in Eq. (3) is due to the hypothesis that $G_S >> G_{gap}$., which is reasonable for short cantilevers where G_S is dominated by the thermal conductance through the cantilever body. Using a thermopile with a sensitivity indicated with s_{TP}, and reading the thermopile voltage with a an amplifier of gain A, the output voltage of the pressure sensor becomes:

$$V_{out} = A \cdot s_{TP} \Delta T \cong \frac{A \cdot s_{TP} G_0}{G_S} W_H \frac{1}{1 + p_{tr} / p} \tag{4}$$

where G_S has been assumed to be due to only the pressure-independent thermal conductivity of cantilever materials. Eq. (4) predicts that the output voltage intrinsically tends to zero with pressure. Therefore, drift and aging effects are much less important with respect to the self-heating structure. This makes the configuration of Fig. 1 (b) more suitable to achieve small detection limit. For both the self and mutual heating configurations, the response tends to saturate when $p >> p_{tr}$ so that the practical operating range does not extend more than a couple of decades over the transition pressure. In order to include the atmospheric pressure into the operating range, p_{tr} should be of the order of a few tens of kPa, requiring gaps of the order of a few microns [8].

2.2) Configuration of the test chip

Two pressure-sensitive structures are placed into a single test-chip that includes a low-noise analog front end (AFE). The chip, whose dimensions are 3.86 x 3.86 mm^2, includes also several flow sensors [26] and acoustical sensors [27], described elsewhere. Both the pressure sensors and the AFE are accessible through dedicated bonding pads. The heaters of the two sensing structures are connected in parallel, to limit the total pad count. Connection between the AFE and one of the sensing structures is accomplished by means of external conductors as shown in Fig. 2, where the configuration used to read sensing structure PS1 is represented. The heaters are biased by low noise current source CS, while voltage source VS biases the negative terminal of the thermopiles, in order to provide a suitable input common mode voltage to the instrumentation amplifier (A). The latter is a low-offset, low-noise chopper amplifier with 46 dB nominal gain, 2 μV maximum input referred offset voltage and 18 nV/√Hz input noise density. Resistor R_S (33 kΩ) is introduced to equalize the resistances seen by the amplifier terminals, reducing the input bias currents (400 pA, maximum) contribution to the input noise [28].

In Fig. 3, a photomicrograph of the portion of the test chip including the AFE and the two pressure sensors is shown. The layout of the AFE is superimposed on the photo to show the electronic circuits buried below the planarization dummies. The magnification shows the two identical sensing structures with the thermopiles and the heaters placed on cantilever beams. Description of the sensing structures and fabrication process is reported in next sub-section.

2.3) Layout of the sensing structures and fabrication approach

The sensing structures, which are based on the configuration of Fig. 1(b), consist of two opposite cantilevers, suspended over a cavity etched into the silicon substrate, as schematically shown in Fig. 4 where the layout and cross section of the device are presented. The cavity has been fabricated with simple micromachining post-processing applied to chip designed with the BCD6s process of

STMicroelectronics. The cantilevers are separated by a 5 μm air-gap (*d* in Fig. 4) and one of them supports a polysilicon heater (1.5 kΩ), while a 10-element *n*-polysilicon/*p*-polysilicon thermopile is placed on the other one. In order to increase the air-gap cross-section, the thick upper aluminum interconnect layer (3 μm thick) has been placed on the tips of both cantilevers obtaining a total thickness of 8.6 μm (*h* in Fig. 4). In this way, the thermal conductance between the two cantilevers is increased with positive effects on the device sensitivity. Furthermore, the thickness of the cantilever supporting the heater has been partially reduced, as shown in Fig.4, exploiting the passivation-opening etching step performed by the silicon foundry. This was aimed at increasing the thermal insulation of the cantilever from the substrate in order to heat the cantilever with less power consumption. The same etching has been used to reduce the thickness of the dielectric stack where the silicon substrate has to be accessed [29].

The main steps of the post-processing are schematically shown in Fig. 5 and the process is similar to that reported in [26]. Briefly, an 8 μm thick photoresist film (MEGAPOSIT™ SPR™ 220–7.0) has been spun onto the chip returned from the silicon foundry. The photoresist layer has been defined to allow the dielectric removal in the cavity area and protect the heater, the thermopile and the rest of the chip, as shown in Fig. 5a. Then, the dielectric layers were etched with a RIE (reactive ion etching) in CF_4/Ar (50%/50%) gas mixture exposing the bare substrate (Fig. 5b). Finally, the silicon substrate has been anisotropically etched for 150 min at 85 °C in a solution of 100 g of 5 wt% TMAH with 2.5 g of silicic acid and 0.7 g of ammonium persulfate (Fig. 5c). Due to the fast degradation of the TMAH solution [29], silicon etching has been performed in three separate 50 min-long steps, each one performed with fresh reagents. In Fig. 6 a SEM micrograph of two sensing structures after the silicon removal is shown. The cavity under the cantilevers is clearly visible.

3. Experimental characterization

3.1) Experimental setup

Experiments have been performed placing the samples inside a vacuum chamber equipped with a turbo pump and a precision, wide range vacuum gauge (Edwards WRG-S). Pressure was initially brought to the minimum value reachable with the given pumping system (10^{-3} Pa). After this step, the vacuum chamber is isolated from the pump by closing a vacuum valve. Air was then introduced in the chamber by means of a needle valve (vent) in order to gradually vary the internal pressure from the minimum value to atmospheric pressure. All measurements were performed in stable conditions (vent and vacuum valve closed). Electrical connections to the sensor chip are shown in Fig. 7. The chips are packaged into DIL28 cases and wedge bonding is used to connect the chip pads to the case pins. The packages are left open in order to expose the chips to the air pressure of the vacuum chamber. The chip pads are connected according to the scheme of Fig. 2, with the exception of the heater pad (V_H), which can be connected to the on-chip current source (position "IN" of switch S_H) as in Fig. 2 or to an external voltage source (position "EX" of switch S_H). The external voltage option is used to characterize the dependence of the output voltage on the heater power, since the internal current source, used for all the other experiments, can be programmed to produce only a total of six distinct current values.

A 3.3 V power supply is provided to the chip by a purposely built Printed Circuit Board, equipped with an ADuC847 microcontroller unit (MCU). The analog output voltage (V_{out}) produced by the chip is read by means of the 24 bit-resolution, 10 Hz bandwidth, delta sigma analog to digital converter (ADC) of the MCU. A Digital to Analog Converter (DAC) is used to produce the external heater voltage. Resistor R_C (100 Ω) is placed in series with the DAC output terminal in order to monitor the heater current, which, together with the heater voltage, is precisely acquired exploiting the multi-input ADC of the MCU. A three-wire SPI interface is used to program a limited set of parameters of the interface. Connection between the MCU board, placed outside the vacuum chamber, and the chip

was accomplished by means of high vacuum electrical feedthroughs. An acquisition program running on a personal computer (PC) controls the MCU board through an USB link.

3.2) Measurement results

All measurements have been performed using a correlated double sampling procedure [30], implemented by taking the difference between two successive V_{out} samples, acquired with the heater turned on and off, respectively. In this way, all residual offset contribution, not due to the heat transfer from the heater to the thermopile hot junctions, is rejected. With heater power, we refer to the power of the individual heaters. Since the heaters of structures PS1 and PS2 are connected in parallel on-chip, they cannot be accessed separately. The individual heater power was then estimated as half of the total power delivered to the combination of the two heaters.

Figure 8 (a) shows the dependence of the output voltage on pressure for structure PS1, at two different heater power settings. It should be observed that the heaters are driven at constant current, so that the actual heating power varies slightly across the displayed pressure range. However, the maximum power variation, estimated by measurement of the heater resistance vs. pressure dependence (shown later in this section), was less than 1 %, so that the approximation of constant power is acceptable. Changing the heater power allows scaling of the output voltage, while the shape of the curve is substantially maintained.

This property can be exploited for implementing auto-range functions, when the voltage increase at high pressures risks saturating the amplifier. According to Eq. (4), we would expect the output voltage to vanish when the pressure tends to zero, while the curves apparently tend to a non-zero asymptotic value, which we will indicate with LAV (Lower Asymptotic Voltage) in the rest of this paper. Figure 8(b) shows a time diagram of the output voltage recorded for a constant pressure of 10^{-3} Pa and 1.1 mW heater power. The noise magnitude superimposed to the LAV mean value is nearly 120 µV peak-to-peak. It is possible to subtract the individual LAV from each curve, partly restoring the voltage decrease at low pressure, as shown in Fig. 9, where this subtraction has been applied to the curves of Fig. 8 (a) and to the same measurements performed on sensing structure PS2 (present on the same test chip).

The experimental V_{out} vs pressure dependence (after LAV subtraction) has been fitted with theoretical expression (4). As an example, Fig. 10 shows the result for structure PS1 in the case of 1.1 mW heater power, for which a transition pressure of nearly 8 kPa has been estimated. Considering all the cases represented in Fig. 9, the transition pressures were found to be in the range 75 kPa± 6 kPa. These values are in good agreement with the p_{tr} vs. gap length experimental relationship proposed in [8].

An interesting result highlighted by Fig. 9 is the very good matching between curves measured on different sensing structures, in spite of the low resolution of the post-processing steps. As can be expected, the characteristics diverge and become erratic when the output voltage gets lower than the noise level, indicated in Fig. 9 by the dashed line. The pressure at which the curves cross the noise level represents the minimum detectable pressure. This limit clearly shifts to lower pressures for higher heater powers. For a power of 1.1 mW, a detection limit of roughly 0.3 Pa can be estimated.

The sensor resolution at any pressure within the measurement range can be obtained by dividing the noise magnitude by the sensitivity, defined as the derivative of the V_{out} vs pressure characteristic. Fig. 11 shows both sensitivity and resolution as a function of pressure for the case W_H=1.1 mW. The sensitivity curve is the average of PS1 and PS2 sensitivities, obtained by numerical differentiation of the corresponding characteristics in Fig. 9. Smoothing is applied to the curves before derivative calculation in order to reduce noise artifacts.

As it is typical of this kind of sensors, the sensitivity starts dropping when pressure becomes comparable with the transition pressure. This causes a progressive resolution degradation from the low-pressure value, which is better than 0.4 Pa, to 50 Pa, exhibited at atmospheric pressure.

In principle, both the resolution and the lower detection limit can be improved by (i) reducing the noise and (ii) increasing the sensitivity. In [26] we have demonstrated that, for the same interface used to read the integrated flow sensors, the output noise is dominated by the thermal (Johnson) noise of the thermopile. This condition applies also to the vacuum sensors of this work, since we are using the same amplifier and the source resistance (thermopile resistance and equalization resistance R_S) is comparable (60 kΩ in both cases). For this reason, noise reduction should necessarily involve reduction of the thermopile resistance. This is generally not an option, unless the width of the cantilever can be enlarged [31], increasing the area occupation and power consumption of the sensing device. Obviously, it is possible to reduce the peak-to-peak noise by filtering the output data stream, e.g. by moving window averaging. The tradeoff in this case is response speed. Sensitivity can be improved by increasing the heater power, as suggested by Eq. (4). In order to verify this possibility, the heater resistance and overheating, estimated from the temperature coefficient of resistance, have been measured as a function of pressure and the result is shown in Fig. 12. It can be seen that the overheating is less than 38 °C suggesting that there is wide margin to reliably increase the heater current in order to improve the sensitivity without degrading the device reliability.

A possible limitation to this approach is due to the amplifier output range that might be exceeded by the output voltage increase caused by boosting the heater power. This problem, which is worst at the highest pressure, can be solved to some extent by reducing the amplifier gain, provided that this operation does not alter the input referred noise of the amplifier. Unfortunately, the LAV is increased by the same factor than the sensitivity, so that, improving the sensitivity via heater power increase does not change the inaccuracy caused by LAV drift occurring after sensor calibration. For this reason, further studies, specifically devoted to gain information on the LAV properties, have been performed and the results are described in next section.

4. Analysis of the lower asymptotic voltage

In order to investigate the mechanisms involved in the LAV, the dependence of the latter on the heater power has been first measured, obtaining the curves (experimental data) shown in Fig. 13. It can be observed that the LAV vanishes for zero heater power, ruling out significant contributions from the amplifier offset. The characteristics are approximately linear, with only a slight upward curvature. This suggests that the LAV is due to parasitic thermal conducting path from the heater to the thermopile tips. These paths should involve mechanisms different from conduction through air gaps, which would be expected to vanish at low pressures. Residual heat transfer should then occur by conduction through solid materials or radiation.
In order to gain further information, we have developed a FEM model with COMSOL software. The geometry of the sensing structure is essentially three-dimensional, so an accurate simulation cannot be performed with a simple 2D model. For this reason, we have developed the 3D model shown in Fig. 14, where the symmetry with respect to the yz-plane passing through x=0 has been used to halve the simulation domain. In order to simplify the model, the stack of dielectric layers that constitute the cantilevers has been considered as a single material. The simulations have been performed using two different modules: the first one models electrical conduction in the heater and allow calculation of the local power dissipation. The results produced by the first module are used as an input for the second module, which models conductive and radiative heat transfer producing the temperature distribution map.
The dependence of the heater resistivity on temperature is taken into account introducing additional coupling between the two modules, which, for this reason, have to be solved simultaneously. As far as radiation is concerned, two different boundary conditions have been applied: i) the surface-to-ambient condition for the top surface of the structure and ii) the surface-to-surface condition for the lateral sides of the cantilevers and the surfaces inside the cavity. The surface-to-ambient radiation assumes that the ambient surroundings in view of the surface behaves as a blackbody at constant

temperature. The surface-to-surface radiation treats the radiative heat exchange between boundaries with automatic view factor calculation.

Validation of the FEM model has been performed comparing the experimental and simulated results in the very low-pressure limit, which was simulated considering the presence of vacuum in the air volume. Since COMSOL Multiphysics does not allow simulations in the molecular regime, it is not possible to perform such a comparison at intermediate pressures. The data that have been taken into account were the heater resistance value and the temperature difference between the hot contact and the cold contact of the thermopile. The experimental resistance values have been precisely estimated from *I-V* curves of the heater measured with a parameter analyzer (HP 4145B). The temperature differences have been estimated from the output signal taking into account the amplifier gain, the number of thermocouples and the Seebeck coefficient of the *p*-poly/*n*-poly thermocouple measured in a previous chip fabricated with the same process [31].

Initial simulations have been performed using the values reported in the COMSOL library for the material properties and assuming silicon dioxide as the material of the stack of dielectric layers. The results obtained in this way showed a significant discrepancy with respect to experimental data. The problem derives from the fact that the COMSOL library data for silicon dioxide are consistent with the properties of bulk fused SiO_2, while the cantilevers are actually formed by a stack of different dielectric layers, such as thermally grown SiO_2, borophosphosilicate glass (BPSG), inter-metal dielectrics and passivation SiO_2/Si_3N_4 mixtures. In order to simplify the model, we have used a single dielectric material, whose properties have been trimmed to match the experimental data. In particular, a thermal conductivity of 1.15 W/mK and a surface emissivity of 0.6 have been adopted. These values are within the range reported in [32] and [33,34], respectively, for dielectrics used in integrated circuit fabrication.

After the described parameter trimming and validation phase, simulation of the dependence of the output voltage on the power delivered to the heater has been performed and the results are plotted in Fig. 13, together with the mentioned experimental results. As it can be seen, a good agreement between simulations and experiments has been obtained even if a slight overestimation of the output voltage at high power is observable. In order to investigate the contribution of radiation, simulations with only the conductive heat transfer has been performed and the result is compared with the other curves in Fig. 13. It is evident that radiation contributes roughly to one third of the output voltage measured at very low pressures, while the remaining part is due to non-uniform temperature of the substrate, caused by heat flow that reaches the substrate itself through the heater cantilever. The well-known nonlinear dependence of radiation on temperature is the cause of the non-linearity of the output voltage at high heater powers.

The same simulations have been performed at atmospheric pressure, treating air as a continuum (no molecular effects) and neglecting convective heat transfer. The simulated results, shown in Fig. 15, are in good agreement with the corresponding experimental data, confirming the validity of the model. In this case, the radiative contribution is negligible, due to prevalent heat conduction through the air.

The LAV dependence on room temperature has been simulated between 273 K (0 °C) and 353 K (80 °C) for three power values. Considering the temperature drift at 298 K, indicated in Fig.16, and the sensitivity shown in Fig. 11, the error introduced by the LAV drift is 50 mPa/K for a heater power of 1.1 mW. Then, for temperature variations up to ± 10 K, the error is still of the same order of the sensor resolution, so that the sensor accuracy is only minimally altered. The total error caused by an 80 K temperature variation is nearly 4.4 Pa.

5. Conclusions

The proposed vacuum sensor is based on mutual heat transfer from a heater to a thermopile across an air gap. This principle, in spite of being intrinsically marked by a much less offset than the traditional approach (self heating), is less popular than the latter for the implementation of integrated Pirani sensors, probably due to the lateral direction (parallel to the chip surface) of heat

transfer, resulting in air gaps of small cross-sections. This drawback, which adversely affects the signal-to-noise ratio at low pressures, has been mitigated in the proposed architecture by exploiting all layers of a standard microelectronic process to obtain an air gap of acceptable vertical extensions (8.6 µm). The very simple post processing procedure used to finish the sensor chips is fully compatible with the original IC fabrication process, as demonstrated by successful integration of an AFE with the sensing structures. As a result of the high precision characteristics of the AFE and use of a CDS procedure, offset and noise contributions from the readout interface have been proven negligible. The sensor resolution, mainly affected by Johnson noise from the thermopile resistance, is better than 0.4 Pa from nearly 0.3 Pa to 1 kPa. Resolution starts degrading beyond this interval, due to the usual sensitivity drop of Pirani-like sensors, although the relative resolution is better than 500 ppm of full-scale up to 100 kPa, giving a feasible operating range of more than 5 decades. FEM simulations showed that at least 30 % of the LAV is due to radiation, which is a strongly temperature dependent phenomenon. However, simulations of the LAV drift suggested that the corresponding error on the pressure reading is close to the sensor resolution for temperature variation of ± 10 K with respect to the calibration temperature. This excellent result is due to the intrinsically small value of the LAV in mutual heating structures. For larger temperature excursion, compensation of the LAV drift could be necessary.

Acknowledgements

References

[1] S. Wilfert, C. Edelmann, Miniaturized vacuum gauges, Journal of Vacuum Science & Technology A 22 (2004) 309-320.

[2] C. Kerkeni, F. BenJemaa, S. Kooli, A. Farhat, M. Maalej, Performance evaluation of a thermodynamic solar power plant: fifteen years of operation history, Renewable Energy 25 (2002) 473–487.

[3] Z. Gan, D. Huang, X. Wang, D. Lin, S. Liu, Getter free vacuum packaging for MEMS, Sensors and Actuators A 149 (2009) 159–164.

[4] I. P. Prikhodko, B. R. Simon, G. Sharma, S. A Zotov, A. A.Trusov, A. M.Shkel, High and Moderate-Level Vacuum Packaging of Vibratory MEMS, in proc. of the 46th International Symposium on Microelectronics, Orlando (FL), USA, Sept. 30 – Oct. 3, 2013, pp. 000705-000710.

[5] E. S. Topalli, K. Topalli, S. E. Alper, T. S., and T. Akin, Pirani Vacuum Gauges Using Silicon-on-Glass and Dissolved-Wafer Processes for the Characterization of MEMS Vacuum Packaging, IEEE Sensors Journal, 9 (2009) 263-270.

[6] A. W. van Herwaarden, P M Sarro, H. C. Meijer, Integrated Vacuum Sensors, Sensors and Actuators, 8 (1985) 187-196.

[7] A. W. van Hervaarden and P. M. Sarro, Double Beam integrated Vacuum Sensors, J. Vac.Sci. Technol. A 5 (1987) 2454-2457.

[8] O. Paul, O. Brand, R. Lenggenhager, H. Baltes, Vacuum gauging with complementary metal–oxide–semiconductor microsensors, Vac. Sci. Technol. A 13, (1995) 503-508.

[9] C. H. Mastrangelo and R. S. Muller, Microfabricated Thermal Absolute-Pressure Sensor with On-Chip Digital Front-End Processor, IEEE J. Solid-State Circuits, 26 (1991) 1998-2007.

[10] J. Wang, Z. Tang, L. Jinfeng Li, Tungsten-microhotplate-array-based pirani vacuum sensor system with on-chip digital front-end processor, Journal of Microelectromechanical Systems 20 (2011): 834-841.

[11] O. Paul, A. Haberli, P. Malcovati, and H. Baltes, Novel Integrated Thermal Pressure Gauge and Read-out Circuit by CMOS IC Technology, in Tech Digest of International Electron Devices Meeting, (IEDM'94), San Francisco, CA, USA, Dec. 11-14, 1994, pp. 131-134.

[12] Jin-Shown Shie, B. C. S. Chou, and Yeong-Maw Chen, High performance Pirani vacuum gauge, J. Vac. Sci. Technol. A 13 (1995) 2972-2979.

[13] M. Doms, A. Bekesch and J. Mueller, A microfabricated Pirani pressure sensor operating near atmospheric pressure, J. Micromech. Microeng. 15 (2005) 1504–1510.

[14] F.T. Zhang, Z. Tang, J. Yu, R.C. Jin, A micro-Pirani vacuum gauge based on micro-hotplate technology, Sensors and Actuators A 126 (2006) 300–305.

[15] J. Mitchell, G. R. Lahiji, and K. Najafi, An Improved Performance Poly-Si Pirani Vacuum Gauge Using Heat-Distributing Structural Supports, J. Microelectromechanical Systems, 17 (2008) 93-102.

[16] F. Santagata, J. F. Creemer, E. Iervolino, L. Mele, A. W. van Herwaarden, P. M. Sarro, A tube-shaped buried pirani gauge for low detection limit with small footprint, J. Microel. Syst. 20 (2011) 676-684.

[17] X. Sun D. Xu, B. Xiong, G. Wu, Y. Wang, A wide measurement pressure range CMOS-MEMS based integrated thermopile vacuum gauge with an XeF_2 dry-etching process, Sensors and Actuators A 201 (2013) 428–433.

[18] Y.-C. Chen, W.-C. Lin, H.-S. Wang, C.-C. Fan, K. C.-H. Lin, B. C. S. Chou, and M. C.-M. Liu, Differential Micro-Pirani Gauge for Monitoring Mems Wafer-Level Package, in proc. of the 28th IEEE International Conference on Micro Electro Mechanical Systems (MEMS), Estoril, Portugal, 18 - 22 January, 2015, pp. 89-92.

[19] M. Grau, F. Völklein, A. Meier, C. Kunz, I. Kaufmann, and P. Woias, Optimized MEMS Pirani sensor with increased pressure measurement sensitivity in the fine and rough vacuum regimes, Journal of Vacuum Science & Technology A 33, (2015) 021601-6.

[20] J.Ruellan, J. Arcamone, D. Mercier, C. Dupré and L. Duraffourg, Pirani gauge based on alternative self-heating of silicon nanowire, in proc of Transducers 2013 & Eurosensors XXVII, Barcelona, Spain, 16-20 June 2013, pp. 2568-2571.

[21] Kourosh Khosraviani and Albert M Leung, The nanogap Pirani-a pressure sensor with superior linearity in an atmospheric pressure range, J. Micromech. Microeng. 19 (2009) 045007-1-8.

[22] Technical Brochure of the 925 Micro Pirani™ vacuum gauge, www.mksinst.com.

[23] P. Bruschi, M. Dei, M. Piotto, A method to compensate the pressure sensitivity of integrated thermal flow sensors, IEEE Sens. J. 10 (2010) 1589–1597.

[24] M. Piotto, A.N. Longhitano, F. Del Cesta, P. Bruschi, Automatic compensation of pressure effects on smart flow sensors in the analog and digital domain, Sensors and Actuators A-Physical 206 (2014) 171-177.

[25] M. Piotto, S. Del Cesta, P. Bruschi, A compact CMOS compatible micro-Pirani vacuum sensor with wide operating range and low power consumption, Procedia Engineering 168 (2016) 766-769 (proc. of EUROSENSORS XXX, Budapest, Hungary, Sept. 4-7, 2016.).

[26] M. Piotto, F. Del Cesta, P. Bruschi, Integrated smart gas flow sensor with 2.6 mW total power consumption and 80dB dynamic range, Microelectronic Engineering 159 (2016) 159-163.

[27] M. Piotto, F. Butti, E. Zanetti, A. Di Pancrazio, G. Iannaccone, P. Bruschi, Characterization and modeling of CMOS-compatible acoustical particle velocity sensors for applications requiring low supply voltages Sensors Actuators A 229 (2015) 192–202.

[28] F. Butti, M. Piotto, and P. Bruschi, A Chopper Instrumentation Amplifier With Input Resistance Boosting by Means of Synchronous Dynamic Element Matching, IEEE Trans. Circuits and Systems–I: Regular Papers, 64 (2017) 753-764.

[29] P. Bruschi, M. Piotto, N. Bacci, Postprocessing, readout and packaging methods for integrated gas flow sensors, Microelectronics Journal 40 (2009) 1300-1307.

[30] C. C. Enz and G. C. Temes, "Circuit techniques for reducing the effects of op-amp imperfections: Autozeroing, correlated double sampling, and chopper stabilization," Proc. IEEE, 84, (1996) 1584–1614.

[31] P. Bruschi and M. Piotto, Design Issues for Low Power Integrated Thermal Flow Sensors with Ultra-Wide Dynamic Range and Low Insertion Loss 3 (2012) 295–314.

[32] M. B. Kleiner, S. A. Kuhn, and W. Weber, Thermal Conductivity Measurements of Thin Silicon Dioxide Films in Integrated Circuits, IEEE Trans. Electron Devices, 43 (1996) 1602-1609.

[33] N. M. Ravindra, S. Abedrabbo, W. Chen, F. M. Tong, A. K. Nanda, and A. C. Speranza, Temperature-Dependent Emissivity of Silicon-Related Materials and Structures, IEEE Trans. on Semiconductor Manufacturing, 11 (1998) 30-29.

[34] F. Völklein, M. Grau, A. Meier, G. Hemer, L. Breuer, and Peter Woias, Optimized MEMS Pirani sensor with increased pressure measurement sensitivity in the fine and high vacuum regime, Journal of Vacuum Science & Technology A 31 (2013) 061604-1-12.

Authors Biographies

Massimo Piotto: Massimo Piotto was born in 1970, La Spezia, Italy. He received his laurea degree in Electronic Engineering from the University of Pisa, Italy, in 1996 and his Ph.D. degree in Electronic, Computer and Telecommunication Engineering in 2000. Since December 2001 he has been a researcher of the "Istituto di Elettronica e di Ingegneria dell'Informazione e delle Telecomunicazioni" - National Research Council (IEIIT-CNR). His main research interests concern MEMS-based smart sensors, microelectronic and nanoelectronic devices and technologies.

Simone Del Cesta: Simone Del Cesta was born in Pisa, Italy, in 1992. He received the Bachelor degree in Biomedical Engineering, in 2013, and the Master degree in Electronic Engineering, in 2015, from the University of Pisa, Italy. He is currently a Ph.D. student in Information Engineering and also an employee of the Sensichips s.r.l start-up since February 2016. He is involved in design of advanced analog circuits for sensor interfacing.

Paolo Bruschi: was born in Massa, Italy, in 1964. He received the Laurea degree in Electronic Engineering from the University of Pisa, Italy, in 1989, and, in 1992, the Perfezionamento degree, equivalent to the Ph.D, from the S. Anna University School of Pisa. In 1993 he joined the Dipartimento di Ingegneria dell'Informazione of the University of Pisa where he is currently an Associate Professor. His main areas of interest are the design of mixed signal integrated circuit and the development of MEMS sensors.

Figure Captions

Figure 1. Structure of micro-Pirani sensors based on self (a) and mutual (b) heating.

Figure 2. Schematic representation of the test chip with the external connections required to read sensing structure PS1 by means of the internal AFE.

Figure 3. Photomicrograph of the test chip portion including the sensing structures and the readout interface (AFE). The magnification shows two identical sensing structures after the silicon etching. The layout of the readout interface is superimposed on the photograph to show the electronic circuits buried below the planarization dummies.

Figure 4. Schematic views of the proposed micro-Pirani: (a) top view and (b) S-S section (not to scale).

Figure 5. Cross section of the sensing structure during the main steps of the post-processing: (a) thick photoresist definition; (b) selective dielectric layer removal with reactive ion etching (RIE); (c) anisotropic silicon etching in a TMAH solution.

Figure 6. SEM micrograph showing the two sensing structures after the anisotropic silicon etching with a TMAH solution.

Figure 7. Sketch of the measurement set-up used to characterize the vacuum sensors.

Figure 8. (a) Output voltage vs. pressure for PS1 sensing structure at two different heater power settings; (b) time diagram of the output voltage for a pressure of 10^{-3} Pa, showing noise.

Figure 9. Output voltage vs. pressure for structures PS1 and PS2 at two different heater power settings, after subtraction of the corresponding low asymptotic values (LAVs).

Figure 10. Result of fitting the response of sensor PS1 for $W_H = 1.1$ mW with Eq. (4), recalled in the legend, where V_A represents a pressure independent factor equal to $As_{TP}G_0W_H/G_S$.

Figure 11. Sensitivity and resolution as a function of pressure. Data represent the average of PS1 and PS2 characteristics measured at $W_H=1.1$ mW.

Figure 12. Heater resistance and overheating as a function of pressure. Overheating has been calculated from the resistance using the temperature coefficient of the heater material (*p*-polysilicon) resistivity, reported in the process design manual.

Figure 13. Output thermopile voltage (amplified by 200) as a function of the power delivered to the heater at a residual pressure of 10^{-2} Pa: comparison between experimental measurements and the simulation results.

Figure 14. Axonometric projection of the 3D COMSOL model used for the FEM numerical simulations

Figure 15. Output thermopile voltage (amplified by 200) as a function of the power delivered to the heater at atmospheric pressure: comparison between experimental measurements and the simulation results. The curves with and without radiation are practically indistinguishable.

Fig.16. Simulation of the LAV dependence on temperature for three different heater powers. The temperature drift at 298 K is indicated.
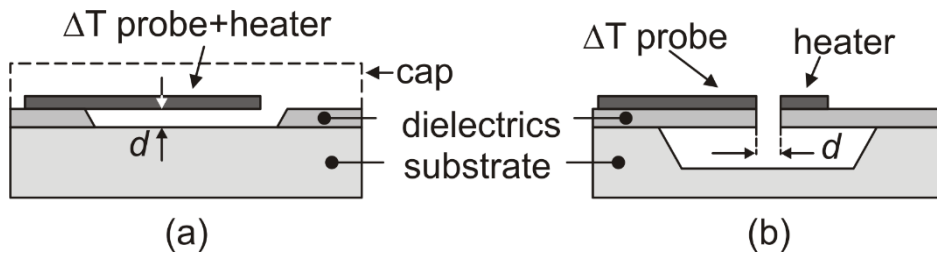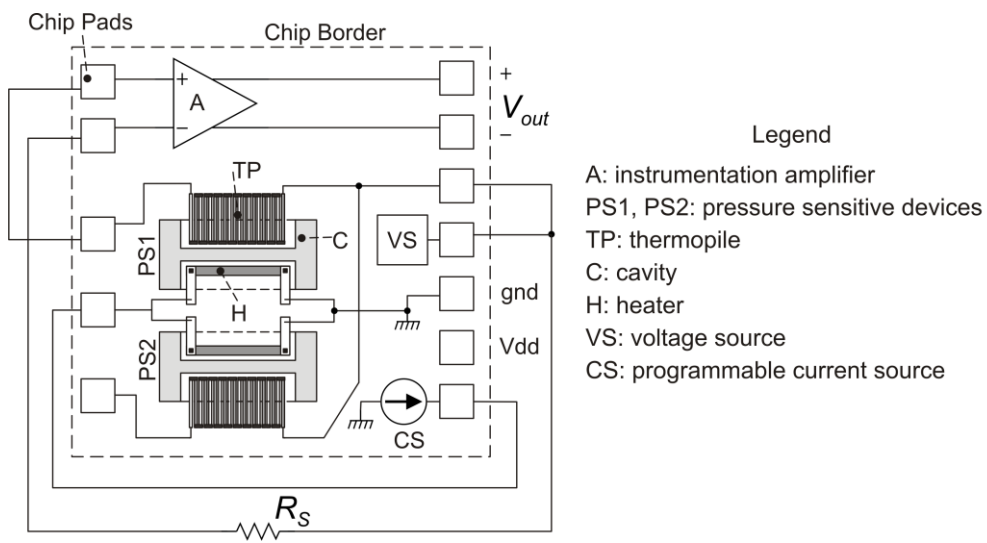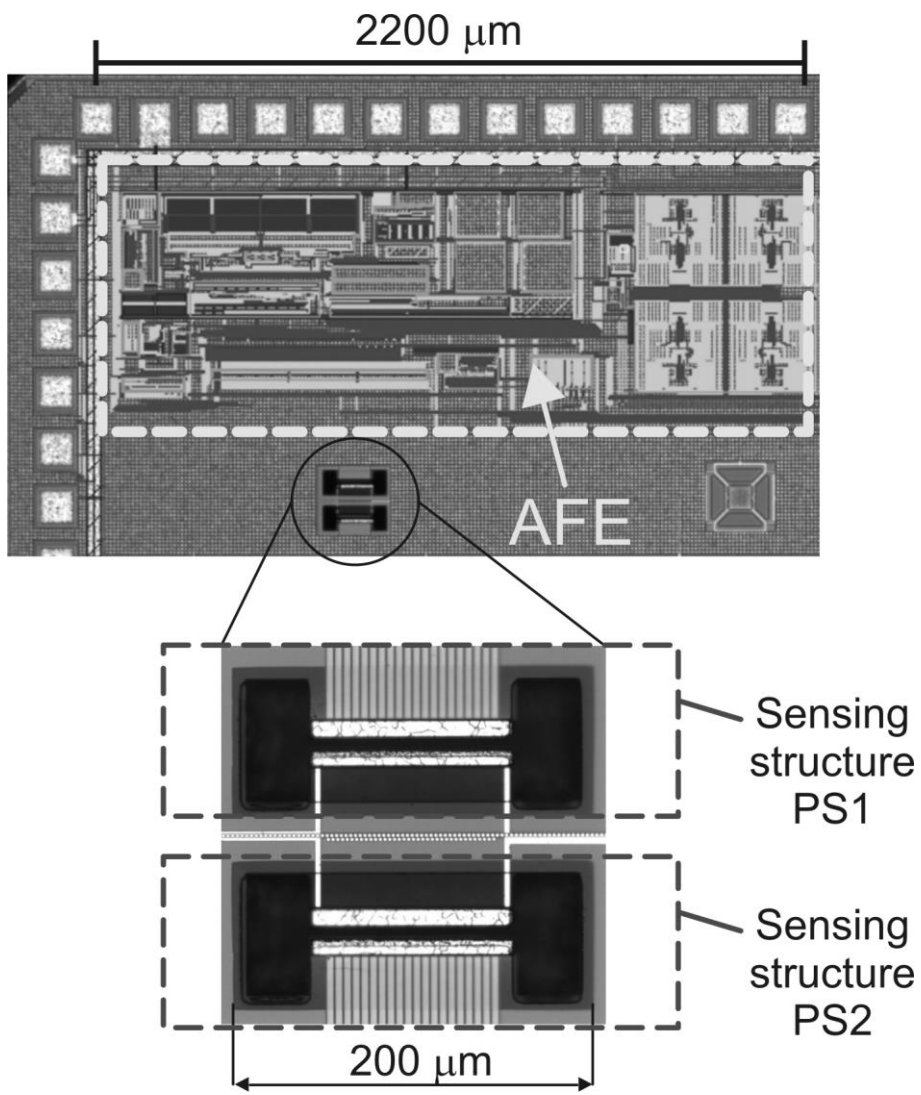
FIGURES

Figure 1

Figure 2

2200 μm

AFE

Sensing structure PS1

Sensing structure PS2

200 μm

Figure 3

Thermopile
(n-poly/p-poly) Cavity Polysilicon
heater SiO$_2$
etching
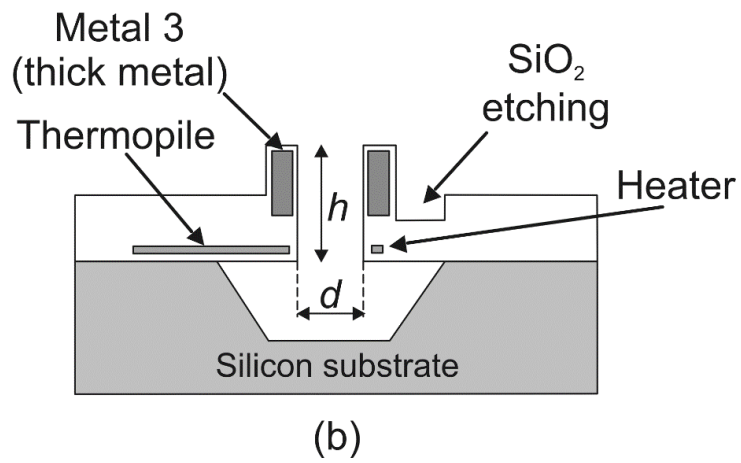
s s

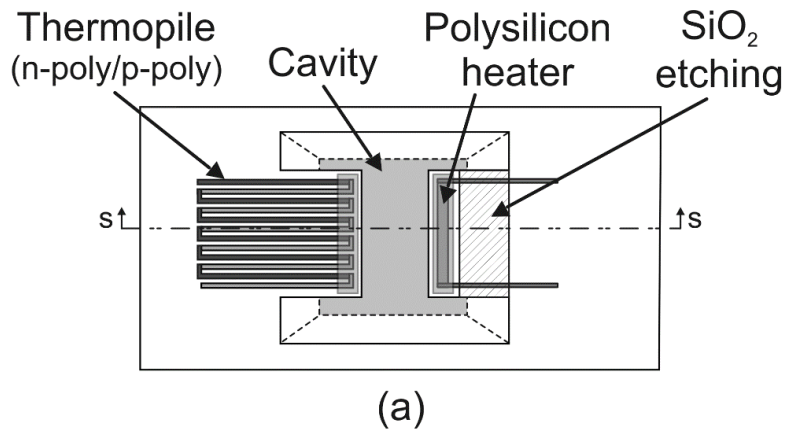(a)

Metal 3
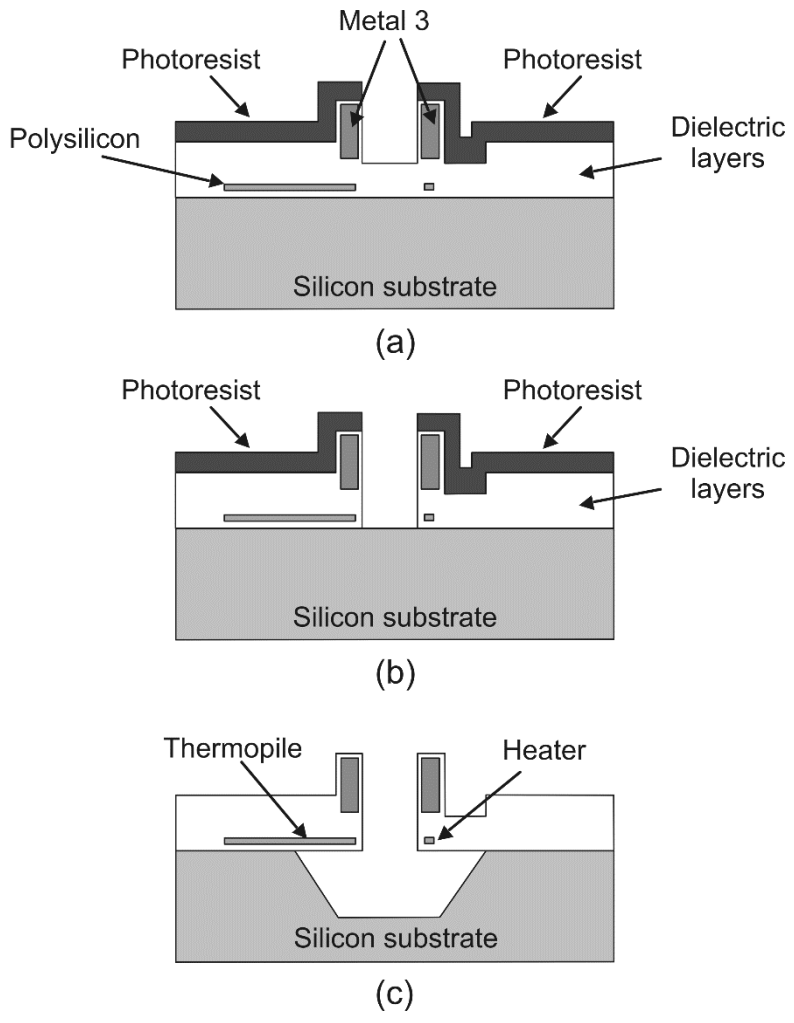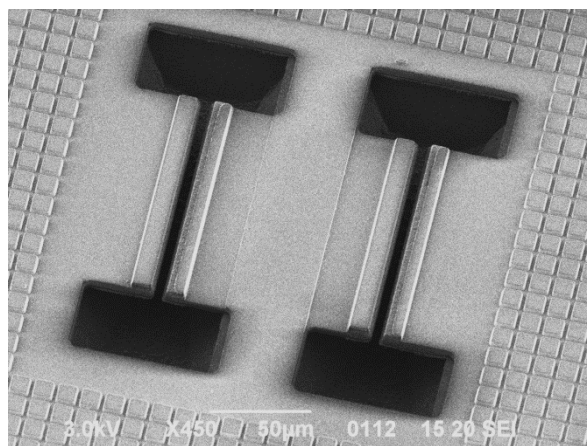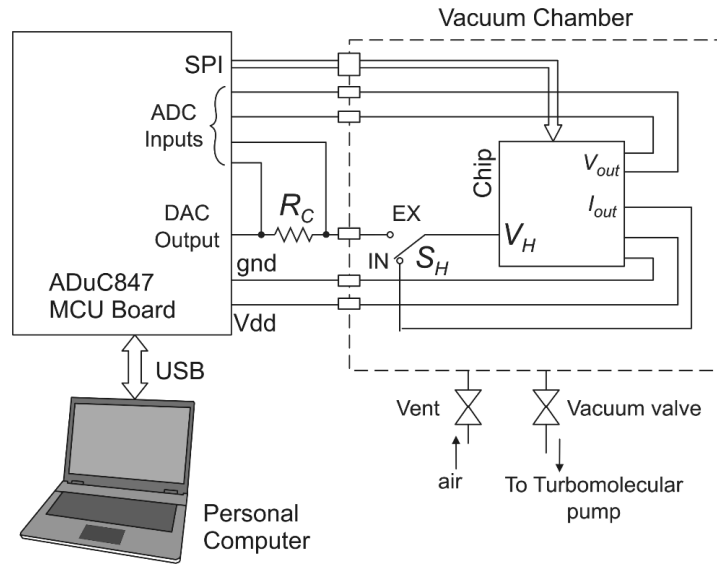(thick metal) SiO$_2$
etching

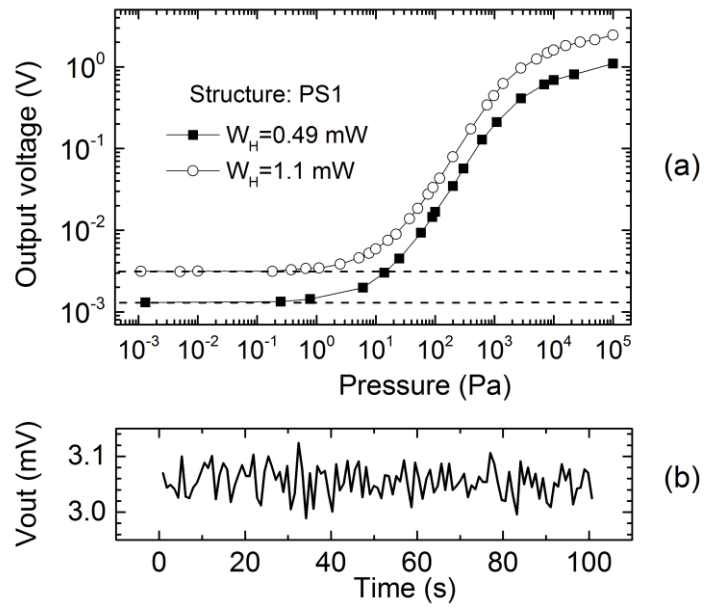Thermopile Heater

h

d

Silicon substrate

(b)

Figure 4

Figure 5
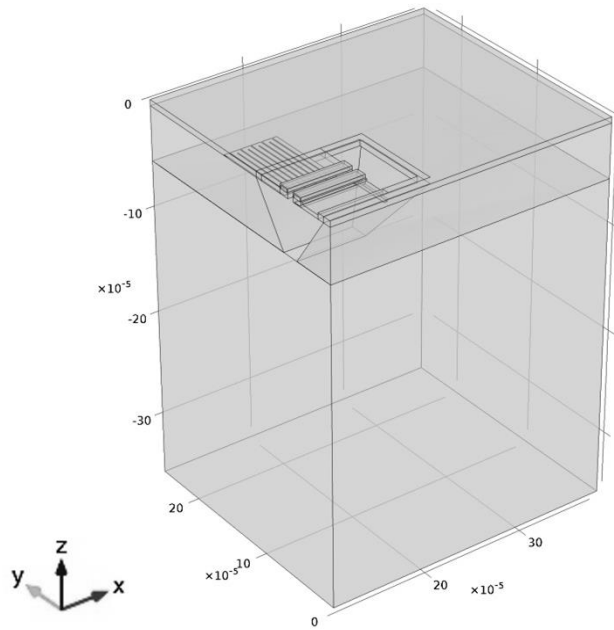

Figure 6
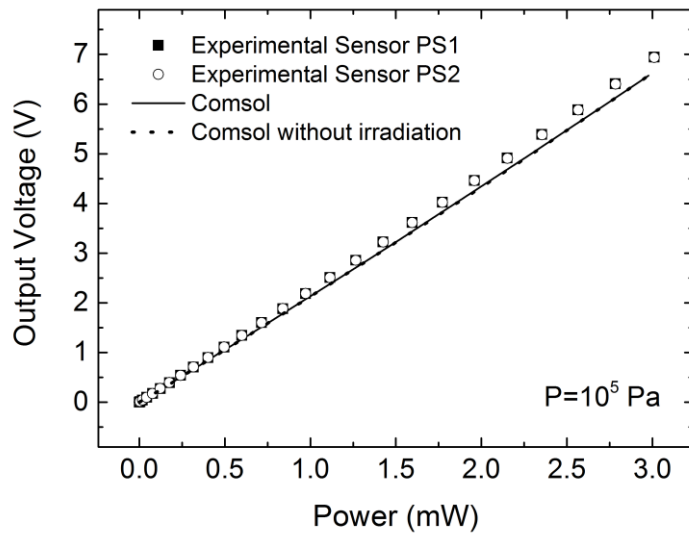
Figure 7
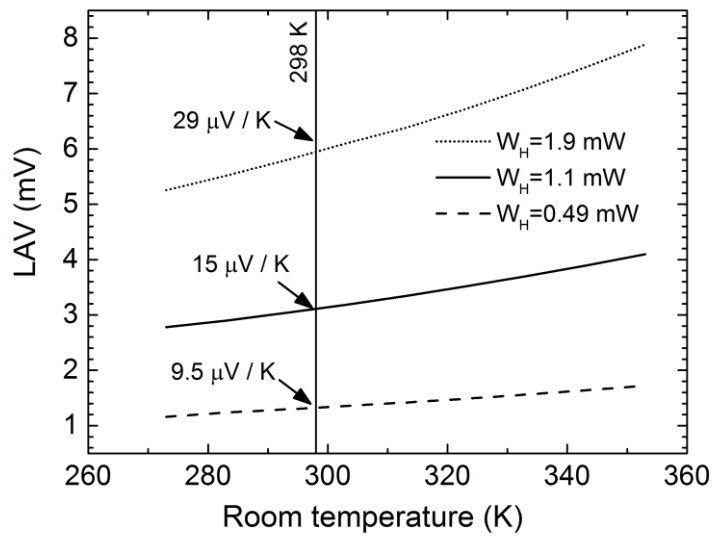

Figure 8
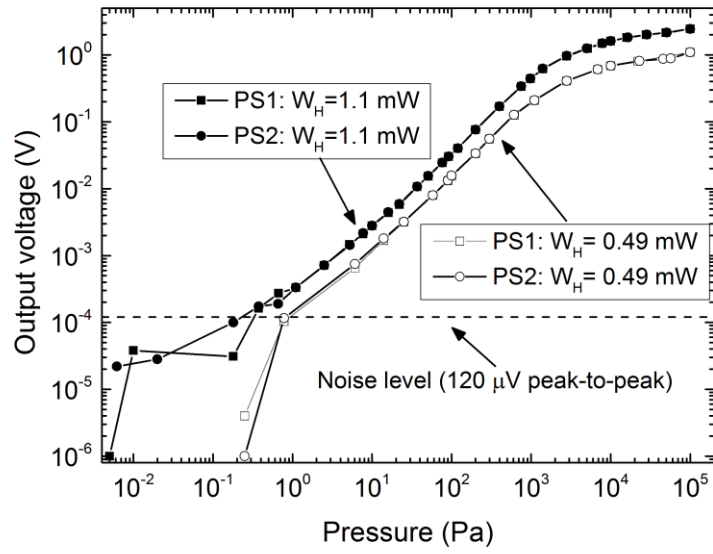
Figure 9
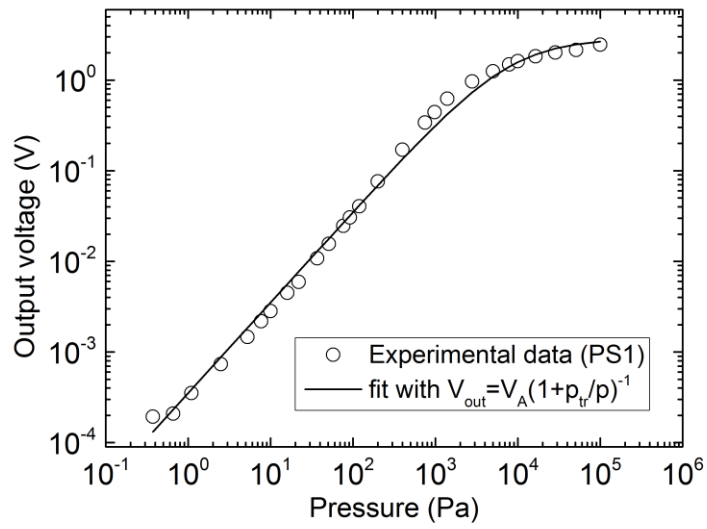
Figure 10
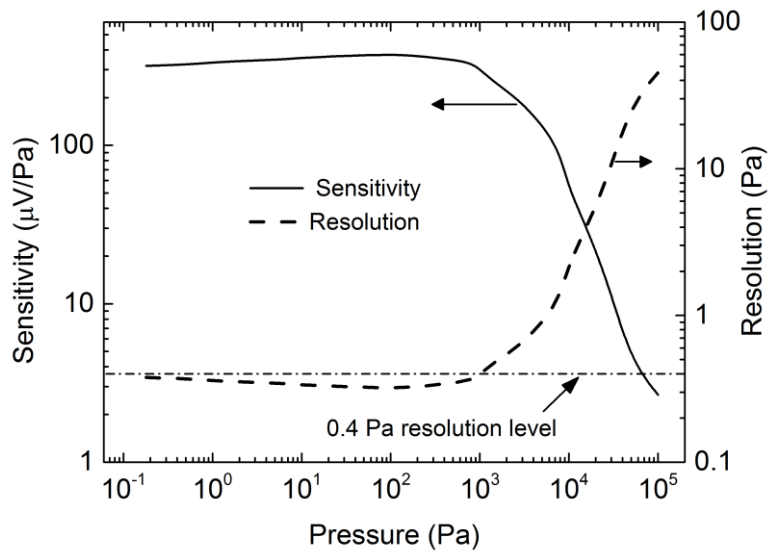
Figure 11
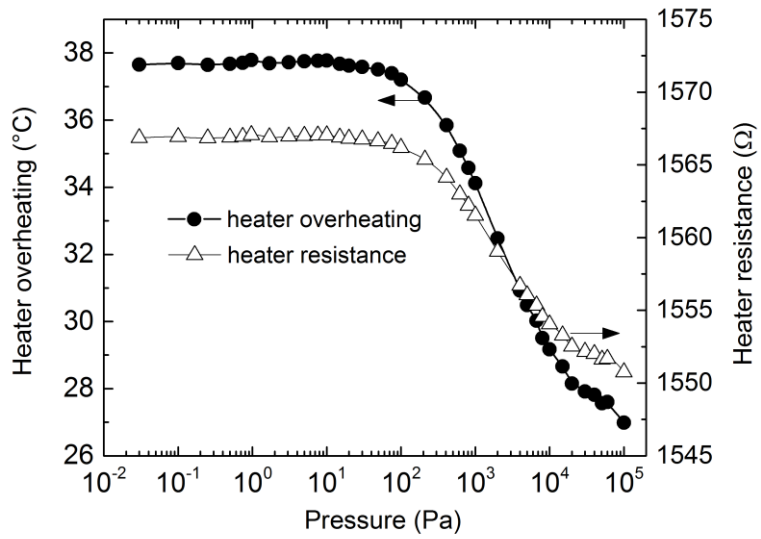
Figure 12
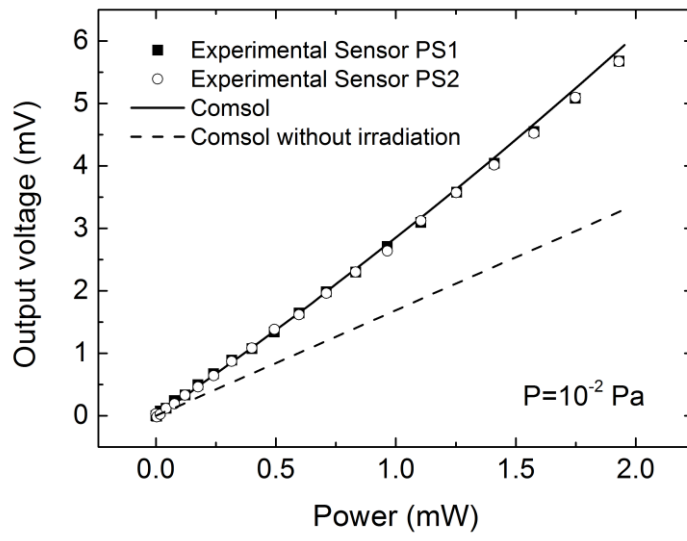
Figure 13

Figure 14

Figure 15

Figure 16